

Deep Plug-and-Play Prior for Massive MIMO Systems

Weixiao Wan, Wei Chen, *Senior Member, IEEE*, Shiyue Wang,
Geoffrey Ye Li, *Fellow, IEEE*, Bo Ai, *Fellow, IEEE*

Abstract—Scalability is a major concern in implementing deep learning (DL) based methods in wireless communication systems. Given various communication tasks, applying one DL model for one specific task is costly in both model training and model storage. In this paper, we propose a novel deep plug-and-play prior method for three communication tasks in the downlink of massive multiple-input multiple-output (MIMO) systems, including channel estimation, antenna extrapolation and channel state information (CSI) feedback. The proposed method corresponding to these three communication tasks employs a common DL model, which greatly reduces the overhead of model training and storage. Unlike general multitask learning, the DL model of the proposed method does not require further fine-tuning for specific communication tasks, but is plug-and-play. Extensive experiments are conducted on the DeepMIMO dataset to demonstrate the convergence, performance, and storage overhead of the proposed method for the three communication tasks.

Index Terms—channel estimation, antenna extrapolation, CSI feedback, deep learning, plug-and-play prior

I. INTRODUCTION

MASSIVE multiple-input multiple-output (MIMO) technology improves system performance by significantly increasing the number of antennas to enhance beamforming gain and reduce inter-user interference, making it a key technology for 5G communication systems [1]. However, with the increase in the number of antennas, the dimension of the wireless channel grows rapidly, which brings huge challenges in various tasks, e.g., channel estimation [2], [3] and channel state information (CSI) feedback [4], [5].

While wireless communication systems continue to develop at a rapid pace, artificial intelligence (AI) technology has also set off a new round of technological revolution. In recent years, deep learning (DL) technology, as a branch of AI, has demonstrated breakthrough performance over classical algorithms in many fields, such as image, video, and natural language processing. AI has been applied for various wireless physical layer tasks in massive MIMO systems and showcases excellent performance [6], [7]. AI based methods have also attracted wide attention in industry, and been considered for standardization. For example, a new study item on AI for new radio air interface has been approved in the 3rd generation

partnership project (3GPP) for beyond 5G (B5G) networks [8].

To deal with different signal processing tasks for massive MIMO, various DL models have been developed. For example, to handle the channel estimation task under massive MIMO. The learned denoising-based approximate message passing (LDAMP) neural network in [9] learns channel features from a large amount of training data and estimates channels, significantly outperforming the compressed sensing (CS)-based methods. In [10], the channel matrix has been modeled as a two-dimensional picture and further processed using a convolutional neural network (CNN) and a denoising network to achieve high accuracy estimation of the channel. Similarly, in the antenna extrapolation task, DNN-based antenna extrapolation for massive MIMO systems in [11] extrapolates downlink CSI from a subset of downlink CSI. Antenna extrapolation via CNN has been implemented in [12] in a reconfigurable intelligent surface (RIS)-assisted communication system. In [13], the neural network structure has been modified by an ordinary differential equation that describes the potential relationships between different data layers and improves the performance of antenna extrapolation. DL techniques have been first applied to CSI feedback in [14], where the DL-based CSI feedback method, namely CsiNet exhibits excellent performance. Afterwards, a large amount of work [15]–[20] has been explored on the basis of CsiNet, mainly in terms of multi-domain correlation extraction utilization, novel neural network structure design, and quantization method improvement to improve the performance of DL-based CSI feedback methods.

DL-based methods have shown superior performance in dealing with various tasks in wireless communication systems, but they bring new challenges. One prominent challenge is the increasing demand for training and storing of different neural network models designed to distinct tasks. Therefore, the existing one-to-one (AI model to communications task) solution is unscalable, and is not suitable for low cost sensors and mobile devices especially.

The adaptability of DL models to different communication tasks and scenarios calls for more investigation. Ideally, it is desired to employ a single DL model to handle multiple communication tasks or scenarios. Therefore, some works have tried to apply multitask learning to communication systems. The multitask training method in [21] improves the adaptability of CSI feedback networks to different channel scenarios; the multitask learning-based precoding network in [22] enhances the adaptability of the network to different signal-to-noise ratios (SNR) of subchannels, which solves the

Weixiao Wan, Wei Chen, Shiyue Wang and Bo Ai are with the State Key Laboratory of Advanced Rail Autonomous Operation, Beijing Jiaotong University, Beijing, China (email: {weixiaowan, weich, shiyuewang, boai} @bjtu.edu.cn).

Geoffrey Ye Li is with the Department of Electrical and Electronic Engineering, Imperial College London, London, U.K (Email: geoffrey.li@imperial.ac.uk).

problem of bit-error rate (BER) loss caused by imperfect CSI. However, multi-task learning usually requires labeled dataset for different tasks, which is not always available or expensive to obtain.

In this paper, we propose a multi-task method based on deep plug-and-play prior (PPP) for massive MIMO systems, which does not require labeled dataset for different tasks. Specifically, we consider three communication tasks including channel estimation, antenna extrapolation, and CSI feedback. Although these tasks are usually formulated as different optimization problems and treated by quite different methods in the literature [9]–[12], [14]–[20], we find that they all exploit the characteristics of the wireless channel. Therefore, we formulate these three tasks as different optimization problems with a common regularization term that acts as the prior of the wireless channel. The main idea is to unroll different different optimization problems into different task-specific subproblems and a common channel-specific subproblem by the variable splitting technique, and solve the common channel-specific subproblem by a common DL based denoiser. By alternating iterative optimization of the task-specific subproblem and the channel-specific subproblem, we could handle the three different tasks with only a single DL model. The proposed method greatly reduces the overhead of model training and storage. Different from general multi-task learning [21], [22], the DL model of the proposed method does not require labeled dataset and further fine-tuning for specific communication tasks.

The remainder of this paper is organized as follows. Section II introduces the system model. Section III presents the proposed method. Section IV provides the experimental results and Section V draws the conclusion.

Notation : Bold uppercase \mathbf{A} and bold lowercase \mathbf{a} denote a matrix and a column vector, respectively, non-bold letter a and A are scalars, blackboard bold letter \mathbb{A} is a set and \mathbb{E} refers specifically to the expectation; Calligraphic letter \mathcal{A} is the mapping, $\|\mathbf{a}\|_2$ is the 2-norm of a vector, $\|\mathbf{A}\|_2$ is the Frobenius norm of a matrix; \mathbf{A}^T , \mathbf{A}^{-1} , \mathbf{A}^H are the transpose, inverse, and hermitian of \mathbf{A} ; \circ represents the hadamard product operator, i.e., the element-by-element multiplication.

II. BACKGROUND AND SYSTEM MODEL

We consider a single-cell massive MIMO orthogonal frequency division multiplexing (OFDM) system operating in the frequency division duplex (FDD) mode. The BS is equipped with N_t antennas with uniform linear array (ULA) arrangement, and the user equipment (UE) is equipped with a single antenna due to limited hardware cost and power consumption. Assume the channel between the UE and the BS consists of L paths. According to the spatially correlated physical channel model in [23], the downlink channel vector $\mathbf{h}_n \in \mathbb{C}^{N_t}$ between the BS and the UE on the n th subcarrier can be expressed as

$$\mathbf{h}_n = \sum_{l=1}^L \alpha_l e^{-j2\pi f_n \tau_l + j\phi_l} \mathbf{a}(\theta_{l,n}), \quad (1)$$

where f_n denotes the subcarrier frequency corresponding to the n th subcarrier, α_l , ϕ_l , and τ_l denote the attenuation coefficient, phase shift, and time delay of the l th path, respectively,

and $\theta_{l,n}$ denotes the angle of arrival (AoA) for the n th subcarrier and the l th path. In addition, $\mathbf{a}(\theta_{l,n})$, the steering vector of the antenna array, is defined as

$$\mathbf{a}(\theta_{l,n}) = \left[1, e^{-j\frac{2\pi d f_n}{c} \sin \theta_{l,n}}, \dots, e^{-j\frac{2\pi d f_n}{c} (N_t-1) \sin \theta_{l,n}} \right]^T, \quad (2)$$

where d denotes the antenna spacing and c is the speed of light. In this paper, we consider three downlink communication tasks, i.e., channel estimation, antenna extrapolation, and CSI feedback. An illustration of the three tasks is shown in Fig. 1.

A. Channel Estimation

As shown in Fig. 1, downlink channel estimation consists of two steps. Firstly, the BS sends allocated pilots for all antennas in different OFDM symbols. Then the UE estimates the downlink channel based on the known pilots and the received signals. Assuming that the OFDM system has N_s subcarriers, the complete downlink CSI $\mathbf{H} \in \mathbb{C}^{N_s \times N_t}$ in the spatial-frequency domain can be expressed as

$$\mathbf{H} = [\mathbf{h}_1, \mathbf{h}_2, \dots, \mathbf{h}_{N_s}]^T. \quad (3)$$

Then the relationship between the transmitted signal and the received signal can be expressed as

$$\mathbf{Y} = \mathbf{H} \circ \mathbf{X} + \mathbf{W}, \quad (4)$$

where $\mathbf{X} \in \mathbb{C}^{N_s \times N_t}$ and $\mathbf{Y} \in \mathbb{C}^{N_s \times N_t}$ denote the transmitted signal and the received signal, respectively, and $\mathbf{W} \in \mathbb{C}^{N_s \times N_t}$ denotes additive white Gaussian noise with mean equal to 0 and variance equal to σ^2 .

To conduct channel estimation, the pilots are usually placed sparsely in a grid of the spatial-frequency domain, and the length of pilots is usually proportional to the number of antennas. For a specific pilot pattern, i.e. positions for pilot signal, the received signal $\mathbf{Y}_p \in \mathbb{C}^{N_{sp} \times N_t}$ at the UE can be expressed as

$$\mathbf{Y}_p = \mathbf{H}_p \circ \mathbf{X}_p + \mathbf{W}_p, \quad (5)$$

where $\mathbf{X}_p \in \mathbb{C}^{N_{sp} \times N_t}$ denotes the transmitted pilots, and $\mathbf{H}_p \in \mathbb{C}^{N_{sp} \times N_t}$ is the channel response at the pilot location. Here, N_{sp} is the number of pilot symbols placed along frequency domain. The relationship between the CSI at pilot positions and the complete downlink CSI \mathbf{H} is given by

$$\mathbf{H}_p = \mathcal{P}(\mathbf{H}), \quad (6)$$

where $\mathcal{P} : \mathbb{C}^{N_s \times N_t} \rightarrow \mathbb{C}^{N_{sp} \times N_t}$ denotes the downsampling operator corresponding to the pilot pattern. In fact, in massive MIMO systems, the pilot positions of different users are usually orthogonal in order to prevent pilot contamination as much as possible. In addition, according to the variation of channel quality, the density of pilots could be adjusted to obtain satisfactory channel estimation performance. Therefore, the pilot patterns used by different users in different communication scenarios could be different in reality, where multiple pilot patterns are configured to fit different communication scenarios.

To sum up, the purpose of downlink channel estimation is to estimate the complete downlink CSI \mathbf{H} with the known pilots

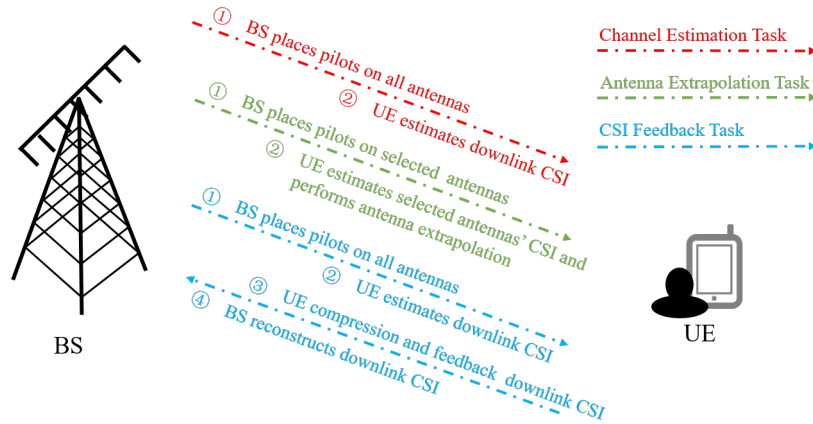


Fig. 1: Schematic diagram of three communication tasks in massive MIMO systems.

\mathbf{X}_p and the received signal \mathbf{Y}_p . The optimization problem can be expressed as

$$\min_{\mathbf{H}} \|\mathbf{Y}_p - \mathcal{P}(\mathbf{H}) \circ \mathbf{X}_p\|_F^2 + \lambda \mathcal{J}(\mathbf{H}), \quad (7)$$

where $\mathcal{J}(\cdot)$ denotes a regularization term that implicitly captures the downlink CSI characteristics and λ is a positive regularization parameter that controls the impact of the regularization term.

Least-squares (LS) estimation and linear minimum mean-squared error (LMMSE) estimation are two classical channel estimation methods. LS estimation is known for its simplicity and convenience, but its estimation accuracy is suboptimal. LMMSE estimation usually achieves enhanced accuracy, but requires second-order channel statistics and noise variance as a priori information, which results in high computational complexity. DL-based channel estimation methods can improve performance [9], [10], [24], [25]. However, the existing methods usually consider a specific pilot pattern, while the corresponding DL model also needs to be replaced by another model if the pilot pattern changes. In the 5G systems, different pilot patterns for various communication scenarios can be configured [26]–[29], which brings huge model training and storage overhead for AI models.

B. Antenna Extrapolation

In massive MIMO systems, the increase in the number of antennas brings higher spatial freedom and multiplexing capability to the system, which results in a huge system performance gain. However, the increase in the number of antennas also brings huge pilot overhead, which is proportional to the number of antennas. In order to reduce the pilot overhead required for channel estimation, a large amount of work has attempted to exploit the correlation between antennas to obtain the CSI of all antennas via only the CSI of selected antennas, known as antenna extrapolation [11]–[13]. However, unlike in the frequency domain, the relationships between the channels in the antenna domain do not have explicit mathematical expressions, even though the channels are highly correlated [11]. Antenna extrapolation can significantly reduce

the pilot overhead, as the pilots can be placed only on selected antennas [30].

As shown in Fig. 1, in the downlink antenna extrapolation task, the BS places pilots on the selected antennas, and the UE estimates the CSI of the selected antennas. The antenna extrapolation is conducted, which can be considered as a post-processing of downlink channel estimation. Assume that the BS selects \bar{N}_t antennas for antenna selection according to an arbitrary antenna selection pattern, then the sampling rate can be defined as $r = \bar{N}_t/N_t$. The relationship between the downlink CSI, $\tilde{\mathbf{H}} \in \mathbb{C}^{N_s \times \bar{N}_t}$, of the selected antennas and the complete CSI, $\mathbf{H} \in \mathbb{C}^{N_s \times N_t}$, of all antennas can be expressed as

$$\tilde{\mathbf{H}} = \mathcal{A}(\mathbf{H}), \quad (8)$$

where $\mathcal{A} : \mathbb{C}^{N_s \times N_t} \rightarrow \mathbb{C}^{N_s \times \bar{N}_t}$ denotes the antenna selection pattern. Here, with reference to the assumptions in [11], the downlink CSI of selected antennas have been perfectly estimated. And we consider the selection of antennas with uniform intervals, although other selection patterns are admitted. Note that different antenna selection patterns will result in different antenna extrapolation performance. The antenna extrapolation can also be formulated as an optimization problem

$$\min_{\mathbf{H}} \|\tilde{\mathbf{H}} - \mathcal{A}(\mathbf{H})\|_F^2 + \lambda \mathcal{J}(\mathbf{H}), \quad (9)$$

where $\mathcal{J}(\cdot)$ denotes the regularization term that implicitly captures the downlink CSI characteristics.

To solve the above optimization problem, in [11], the proposed DL model is trained for a specific antenna selection pattern. If the antenna selection pattern is changed, the DL model would no longer be valid. This drawback has also been noticed and discussed in the literature [12], [13], [31].

C. CSI Feedback

In FDD massive MIMO systems, the BS needs accurate downlink CSI [32] to perform precoding and beamforming. As shown in Fig. 1, once the UE obtains the downlink CSI \mathbf{H} , some form of information needs to be fed back to the BS. To reduce feedback overhead, a two-dimensional discrete

Fourier transform (DFT) is employed to transform the CSI into the angular-delay domain, which leads to

$$\check{\mathbf{H}} = \mathbf{F}_s \mathbf{H} \mathbf{F}_t, \quad (10)$$

where \mathbf{F}_s and \mathbf{F}_t are the DFT matrices of dimension $N_s \times N_s$ and $N_t \times N_t$, respectively. As the large CSI coefficients in the angular-delay domain occupy only a small portion and the other coefficients are close to zero, the angular-delay domain downlink CSI $\check{\mathbf{H}}$ is sparse. Moreover, since the time delay between multipath arrivals at the UE is in a finite period, almost all large coefficients are in the first \bar{N}_s rows of $\check{\mathbf{H}}$. Therefore, the first \bar{N}_s rows of $\check{\mathbf{H}}$, denoted as $\bar{\mathbf{H}} \in \mathbb{C}^{\bar{N}_s \times N_t}$, are fed to the BS and the rest of the rows are simply ignored to reduce the feedback overhead in [14].

To further reduce the feedback overhead, various DL based methods have been proposed to compress the angular-delay domain downlink CSI. The mostly considered DL architecture for CSI compression is the autoencoder, where the UE and the BS use a DL-based encoder and a DL-based decoder, respectively [14]–[17], [33]. The encoder DL model at the UE maps $\bar{\mathbf{H}}$ to a low-dimensional compressed space, while the decoder DL model at the BS maps the received feedback information to the original dimension to construct $\bar{\mathbf{H}}$. However, the two-sided DL model at both the UE and the BS has several drawbacks. First, the use of DL technique comes at the considerable cost of computational complexity and model storage overhead, which severely hinders its use in low-cost UE, such as IoT devices. Second, joint training of the two-sided DL model requires consensus and collaborations between the BS and the UE, which is not easy to achieve in practice considering the standardization issues.

To overcome these shortcomings, a one-sided CSI feedback framework is proposed in [34], where only the BS-side requires the deployment of DL models. On the UE side, the CSI is simply compressed by linear mapping, which can significantly reduce the computational burden on the UE side and eliminate the need for collaborations. In the one-sided CSI feedback framework, the compression process at the UE side can be expressed as

$$\mathbf{y} = \mathbf{A} \bar{\mathbf{h}} + \mathbf{w}, \quad (11)$$

where $\bar{\mathbf{h}} \in \mathbb{R}^N$ consists of the real and imaginary parts of the truncated angular-delay domain CSI $\bar{\mathbf{H}}$ spliced after vectorization, $N = 2\bar{N}_s N_t$, $\mathbf{y} \in \mathbb{R}^M$, $\mathbf{A} \in \mathbb{R}^{M \times N}$ denote the compressed CSI vector and the linear projection matrix, respectively, and $\mathbf{w} \in \mathbb{R}^M$ denotes the quantization noise caused by the quantization process. The dimension M of the compressed CSI vector \mathbf{y} is usually much smaller than the dimension N of the CSI vector $\bar{\mathbf{h}}$, so the compression ratio $\text{CR} = M/N$ is much lower than 1. The CSI reconstruction problem at the BS side can be formulated as

$$\min_{\bar{\mathbf{h}}} \|\mathbf{y} - \mathbf{A} \bar{\mathbf{h}}\|_2^2 + \lambda \mathcal{J}(\bar{\mathbf{h}}), \quad (12)$$

where $\mathcal{J}(\cdot)$ denotes the regularization term that implicitly captures the angular-delay properties of the channel response by using the CSI vector $\bar{\mathbf{h}}$ as a priori information.

III. MULTI-TASK DEEP PPP

In this section, we propose a multi-task deep PPP method that employs a common DL model to handle different tasks in massive MIMO systems including channel estimation, antenna extrapolation, and CSI feedback. We first introduce the deep PPP method to solve linear inverse problems and the design perspectives of DL-based denoiser. Then we provide the details about how the three communication tasks formulated in Section II can be solved.

A. Deep PPP

The three communication tasks formulated in Section II boil down into linear inverse problems. Mathematically, the so-called linear inverse problem is to recover the unknown signal $\mathbf{x} \in \mathbb{R}^N$ from the observed data $\mathbf{y} \in \mathbb{R}^M$ by a known linear observation mapping $\mathcal{T}(\cdot)$, and the observed data are usually corrupted by some noise $\mathbf{n} \in \mathbb{R}^M$, given by

$$\mathbf{y} = \mathcal{T}(\mathbf{x}) + \mathbf{n}. \quad (13)$$

The recovery of \mathbf{x} from observation data \mathbf{y} can be formulated as the following optimization problem

$$\min_{\mathbf{x}} \|\mathbf{y} - \mathcal{T}(\mathbf{x})\|_2^2 + \lambda \mathcal{J}(\mathbf{x}), \quad (14)$$

where $\|\mathbf{y} - \mathcal{T}(\mathbf{x})\|_2^2$ is the data-fidelity term that captures the difference between the recovered signal and the original signal, $\mathcal{J}(\cdot)$ is the regularization term that captures priori signal information, and λ is the positive regularization parameter that promotes the balance between the data-fidelity term and the regularization term. In specific, for the three communication tasks described in Section II, the data-fidelity terms corresponding to channel estimation, antenna extrapolation and CSI feedback are $\|\mathbf{Y}_p - \mathcal{P}(\mathbf{H}) \circ \mathbf{X}_p\|_F^2$, $\|\tilde{\mathbf{H}} - \mathcal{A}(\mathbf{H})\|_F^2$ and $\|\mathbf{y} - \mathbf{A} \bar{\mathbf{h}}\|_2^2$, respectively.

In order to solve the above optimization problem, variable splitting algorithms such as alternating direction method of multipliers (ADMM) and half-quadratic splitting (HQS) could be employed. As HQS is concise and converges quickly [35], we use HQS to decouple the data-fidelity term from the regularization term. By introducing an auxiliary variable \mathbf{z} , the optimization problem in (14) can be rewritten as

$$\begin{aligned} \min_{\mathbf{x}} \quad & \|\mathbf{y} - \mathcal{T}(\mathbf{x})\|_2^2 + \lambda \mathcal{J}(\mathbf{x}) \\ \text{s.t.} \quad & \mathbf{z} = \mathbf{x}. \end{aligned} \quad (15)$$

The Lagrangian function is given by

$$\mathcal{L}_\rho(\mathbf{x}, \mathbf{z}) = \|\mathbf{y} - \mathcal{T}(\mathbf{x})\|_2^2 + \lambda \mathcal{J}(\mathbf{x}) + \rho \|\mathbf{z} - \mathbf{x}\|_2^2, \quad (16)$$

where $\|\mathbf{z} - \mathbf{x}\|_2^2$ is the constraint term and ρ is the positive penalty parameter. By gradually increasing ρ , the solution of (16) will get close to the solution of (15). The optimization problem in (16) can be solved by iteratively solving the subproblems with variables \mathbf{z} and \mathbf{x} in turn, which is expressed as

$$\begin{cases} \mathbf{x}^{t+1} := \arg \min_{\mathbf{x}} \|\mathbf{y} - \mathcal{T}(\mathbf{x})\|_2^2 + \rho \|\mathbf{z}^t - \mathbf{x}\|_2^2, & (17a) \\ \mathbf{z}^{t+1} := \arg \min_{\mathbf{z}} \mathcal{J}(\mathbf{z}) + \frac{1}{2 \left(\sqrt{\frac{\lambda}{2\rho}}\right)^2} \|\mathbf{z} - \mathbf{x}^{t+1}\|_2^2. & (17b) \end{cases}$$

Algorithm 1: Solving Linear Inverse Problem via PPP.

Input: Observed data \mathbf{y} , linear observation mapping $\mathcal{T}(\cdot)$, regularization parameters λ , penalty factor ρ , scaling factor α , number of iterations N

Output: Reconstructed signal $\hat{\mathbf{x}}$

- 1 Initialize input data \mathbf{z}^1
- 2 **for** $t = 1 : N$ **do**
- 3 Compute \mathbf{x}^{t+1} by (17a)
- 4 Compute \mathbf{z}^{t+1} by (18)
- 5 Update penalty factor $\rho^{t+1} = \alpha\rho^t$;
- 6 **end**
- 7 **return** \mathbf{x}^{N+1}

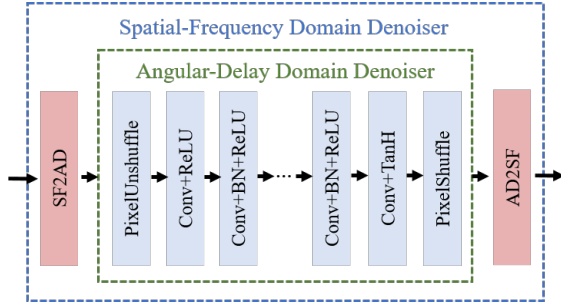


Fig. 2: Schematic diagram of the denoising network structure.

The subproblem in (17a) leads to the proximal solution, \mathbf{x}^{t+1} , which usually has a closed-form solution owing to linear mapping $\mathcal{T}(\cdot)$. The subproblem in (17b) can be seen as the Maximum A Posteriori (MAP) estimation problem, where the prior of \mathbf{z} is $e^{-\mathcal{J}(\mathbf{z})}$ and \mathbf{z} is corrupted by a Gaussian noise with variance $\sigma^2 = \frac{\lambda}{2\rho}$. Thus, a denoiser can be used to solve (17b) implicitly, which can be rewritten as follows

$$\mathbf{z}^{t+1} = \text{Denoiser}\left(\mathbf{x}^{t+1}, \sigma^2 = \frac{\lambda}{2\rho}\right). \quad (18)$$

Note that the parameters, ρ and λ , are involved in the whole alternating iterative optimization process, and the setting of the two parameters affects convergence. To ensure that \mathbf{x}^{t+1} and \mathbf{z}^{t+1} converge to a fixed point, ρ , i.e., the weight of the constraint term, needs to keep getting larger during the iterative process. The increase of ρ can be also viewed as the decrease of the noise variance in (18), and \mathbf{x}^{t+1} and \mathbf{z}^{t+1} will gradually converge to the true value. The process on solving linear inverse problem via PPP is summarized in the algorithm 1.

According to the optimization process discussed above, the noise variance in (18) changes continuously during the iterative process, which means that the denoiser needs to have the ability to handle a varying noise level. In this paper, we design a DL-based denoiser that can be used simultaneously for the three communication tasks, i.e., channel estimation, antenna extrapolation, and CSI feedback. In specific, the channel estimation problem in (7) and the antenna extrapolation problem in (9) directly deal with the downlink CSI \mathbf{H} in the spatial-frequency domain, while the CSI feedback problem

in (12) deals with the tailored CSI $\check{\mathbf{H}}$ in the angular-delay domain, which exploits the limited time delay of multi-path to reduce redundancy. To deal with the channel in different domains, we consider a denoising network with a structure shown in Fig 2. The DL-based denoiser works in the angular-delay domain. The SF2AD module is applied before the denoiser, which converts the spatial-frequency CSI into the angular-delay domain CSI $\check{\mathbf{H}}$ by 2D DFT, and truncates the part with small elements to obtain the truncated angular-delay domain CSI $\bar{\mathbf{H}}$ for denoising, which can be expressed as

$$\bar{\mathbf{H}} = \text{SF2AD}(\mathbf{H}) = f_{\text{cropping}}(\text{DFT}(\mathbf{H})), \quad (19)$$

where $f_{\text{cropping}}(\cdot)$, a cropping function, crops off the part of the angular-delay domain CSI $\check{\mathbf{H}}$ with small elements. The AD2SF module feed zeros back into the truncated angular-delay domain CSI after denoising, and then converts it to the spatial-frequency domain by 2D IDFT. The process is expressed as

$$\mathbf{H} = \text{SF2AD}(\bar{\mathbf{H}}) = \text{IDFT}(f_{\text{padding}}(\bar{\mathbf{H}})), \quad (20)$$

where $f_{\text{padding}}(\cdot)$ denotes the zero-padding function that zero-pads the cropped part to the original dimension. By using the SF2AD and the AD2SF modules, the DL-based denoiser originally designed for the CSI in angular-delay domain can be reused to deal with CSI in spatial-frequency domain.

The DL model structure is shown in the blue box in Fig. 2. The first layer of the denoiser is the pixel unshuffle layer, followed by several convolutional layers to extract features, and finally restored to the original dimension by the pixel shuffle layer. Considering the balance between the computational complexity of the network and the denoising performance, we set up 8 convolutional layers in the middle convolutional operation, and each convolutional layer has 48 convolutional kernels. The denoiser can be expressed as

$$\hat{\mathbf{H}} = \text{Denoiser}\left(\check{\mathbf{H}}, \sigma^2; \Theta\right), \quad (21)$$

where Θ denotes the set of parameters of the DL-based denoiser and σ^2 denotes the noise variance. To learn the model parameters Θ from a noisy CSI dataset, the loss function for training this denoiser is given by

$$\mathcal{L}(\Theta) = \frac{1}{T} \sum_{j=1}^T \frac{\left\| \bar{\mathbf{H}}_j - \text{Denoiser}\left(\check{\mathbf{H}}_j, \sigma^2; \Theta\right) \right\|_F^2}{\left\| \bar{\mathbf{H}}_j \right\|_F^2}, \quad (22)$$

where T is the total number of samples in the training set, subscript j denotes the j th sample in the training set, and $\|\cdot\|_F$ denotes the Frobenius norm. Note that the common DL-based denoiser can be trained off-line and applied to all the three tasks in the inference stage.

B. Channel Estimation via Deep PPP

This subsection describes the proposed algorithm, i.e., PP-PCE, for the downlink channel estimation task. According to (7) and (16), the subproblem in (17a) can be rewritten as

$$\mathbf{H}^{t+1} := \arg \min_{\mathbf{H}} \left\| \mathbf{Y}_p - \mathcal{P}(\mathbf{H}) \circ \mathbf{X}_p \right\|_F^2 + \rho \left\| \mathbf{Z}^t - \mathbf{H} \right\|_F^2, \quad (23)$$

Algorithm 2: PPPCE.

Input: Transmitted pilots \mathbf{X}_p , received pilots \mathbf{Y}_p , pilot pattern $\mathcal{P}(\cdot)$, regularization parameters λ , penalty factor ρ , scaling factor α , number of iterations N

Output: Estimated downlink CSI $\hat{\mathbf{H}}$

```

1 Initialization by LS estimation, get  $\mathbf{Z}^1$ 
2 for  $t = 1 : N$  do
3   Compute  $\mathbf{H}^{t+1}$  by (24)
4   Convert  $\mathbf{H}^{t+1}$  to the angular-delay domain and
   truncate it by SF2AD module
5   Compute  $\mathbf{Z}^{t+1}$  by (21)
6   Convert  $\mathbf{Z}^{t+1}$  to the spatial-frequency domain by
   AD2SF module with zero padding
7   Update penalty factor  $\rho^{t+1} = \alpha\rho^t$ ;
8 end
9 return  $\mathbf{Z}^{N+1}$ 

```

Algorithm 3: PPPAE.

Input: The selected antennas' downlink CSI $\tilde{\mathbf{H}}$, antenna selection pattern $\mathcal{A}(\cdot)$, regularization parameters λ , penalty factor ρ , scaling factor α , number of iterations N

Output: Extrapolated downlink CSI $\hat{\mathbf{H}}$

```

1 Initialization by spline interpolation, get  $\mathbf{Z}^1$ 
2 for  $t = 1 : N$  do
3   Compute  $\mathbf{H}^{t+1}$  by (26)
4   Convert  $\mathbf{H}^{t+1}$  to the angular-delay domain and
   truncate it by SF2AD module
5   Compute  $\mathbf{Z}^{t+1}$  by (21)
6   Convert  $\mathbf{Z}^{t+1}$  to the spatial-frequency domain by
   AD2SF module with zero padding
7   Update penalty factor  $\rho^{t+1} = \alpha\rho^t$ ;
8 end
9 return  $\mathbf{Z}^{N+1}$ 

```

which has a closed-form solution as following

$$h_{ij}^{t+1} = \begin{cases} \frac{x_{ij}y_{ij} + \rho z_{ij}^t}{x_{ij}^2 + \rho}, & (i, j) \in \mathbb{P} \\ z_{ij}^t, & (i, j) \in \bar{\mathbb{P}}, \end{cases} \quad (24)$$

where h_{ij} , x_{ij} , y_{ij} , and z_{ij}^t denote the (i, j) -th element in the CSI \mathbf{H} , corresponding element in the transmitted pilots \mathbf{X}_p , corresponding element in the received pilots \mathbf{Y}_p , and the (i, j) -th element in the denoising result in the t th iteration \mathbf{Z}^t , respectively. The sets \mathbb{P} and $\bar{\mathbb{P}}$ denote the pilot and non-pilot positions, respectively. The proof of (24) can be found in Appendix A.

Subproblem (17b) can be solved by the DL-based denoiser described in the previous subsection. The proposed plug-and-play channel estimation algorithm, i.e., PPPCE, is shown in Algorithm 2, where the LS estimation is used for initialization. Note that PPPCE can be used for arbitrary pilot patterns since the DL-based denoiser works on the angular-delay domain and is decoupled from the configuration of the pilot patterns.

C. Antenna Extrapolation via Deep PPP

This subsection describes the proposed algorithm, i.e., PPPAE, for the downlink antenna extrapolation task. According to (9), (15), and (16), subproblem (17a) for the antenna extrapolation task can be expressed as

$$\mathbf{H}^{t+1} := \arg \min_{\mathbf{H}} \left\| \tilde{\mathbf{H}} - \mathcal{A}(\mathbf{H}) \right\|_F^2 + \rho \left\| \mathbf{Z}^t - \mathbf{H} \right\|_F^2. \quad (25)$$

Its closed-form solution is given by

$$h_{ij}^{t+1} = \begin{cases} \frac{\tilde{h}_{ij} + \rho z_{ij}^t}{1 + \rho}, & (i, j) \in \mathbb{A} \\ z_{ij}^t, & (i, j) \in \bar{\mathbb{A}}, \end{cases} \quad (26)$$

where h_{ij} , \tilde{h}_{ij} , and z_{ij}^t denote the (i, j) -th elements in the full CSI \mathbf{H} , corresponding element in observed CSI $\tilde{\mathbf{H}}$ and the (i, j) -th elements in the result of the denoiser in the t th iteration \mathbf{Z}^t , respectively. The sets \mathbb{A} and $\bar{\mathbb{A}}$ denote the selected antenna and unselected antenna positions, respectively, and the proof of (26) can be referred to in Appendix B.

Subproblem (17b) can be solved by the DL-based denoiser in the subsection III-A. Algorithm 3 shows the plug-and-play antenna extrapolation, i.e., PPPAE. The results obtained from the spline interpolation are used as the initialization. The DL model in the PPPAE can be used for any antenna selection patterns, while the existing DL-based antenna extrapolation methods [11] can only deal with fixed antenna selections and several DL models need to be trained and stored to work on different antenna selection patterns.

D. CSI Feedback via Deep PPP

This subsection describes the proposed algorithm PPPCF for the CSI feedback task. According to (12), (15), and (16), subproblem (17a) under the CSI feedback task can be expressed as

$$\bar{\mathbf{h}}^{t+1} := \arg \min_{\bar{\mathbf{h}}} \left\| \mathbf{y} - \mathbf{A}\bar{\mathbf{h}} \right\|_2^2 + \rho \left\| \mathbf{z}^t - \bar{\mathbf{h}} \right\|_2^2. \quad (27)$$

For this unconstrained optimization problem, the closed-form solution is given by

$$\bar{\mathbf{h}}^{t+1} = (\mathbf{A}^T \mathbf{A} + \rho \mathbf{I})^{-1} (\mathbf{A}^T \mathbf{y} + \rho \mathbf{z}^t), \quad (28)$$

where \mathbf{I} is the identity matrix. Unlike (24) and (26), the computational complexity of (28) is large due to the inverse of the high-dimensional matrix. In order to reduce the computational complexity of (28), we simplify the operation by performing singular value decomposition of the linear mapping matrix \mathbf{A} in (28), and the simplified closed-form solution can be expressed as

$$\bar{\mathbf{h}}^{t+1} = \left(\mathbf{V}^T \begin{bmatrix} \frac{1}{1+\rho} \mathbf{I} & \mathbf{0} \\ \mathbf{0} & \frac{1}{\rho} \mathbf{I} \end{bmatrix} \mathbf{V} \right) (\mathbf{A}^T \mathbf{y} + \rho \mathbf{z}^t), \quad (29)$$

where \mathbf{V}^T is the right unitary matrix obtained after the SVD of linear mapping matrix \mathbf{A} . The derivation of (29) is given in Appendix C. Although penalty factor ρ is constantly updated iteratively, we avoid computing the matrix inverse for each iteration.

Algorithm 4: PPPCF.

Input: The compressed CSI vector \mathbf{y} , linear mapping matrix \mathbf{A} , regularization parameters λ , penalty factor ρ , scaling factor α , number of iterations N

Output: Reconstructed CSI vector $\hat{\mathbf{h}}$

- 1 Initialization, get \mathbf{z}^1
- 2 **for** $t = 1 : N$ **do**
- 3 Compute $\bar{\mathbf{h}}^{t+1}$ by (29)
- 4 Compute \mathbf{z}^{t+1} by (21)
- 5 Update penalty factor $\rho^{t+1} = \alpha\rho^t$;
- 6 **end**
- 7 **return** \mathbf{z}^{N+1}

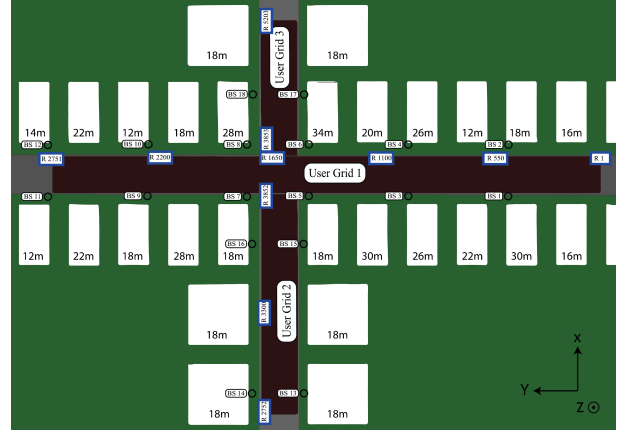


Fig. 3: Schematic diagram of O1_28 scenario [36].

Unlike channel estimation and antenna extrapolation, the iterative process of CSI feedback is performed on the angular-delay domain. Therefore, the denoiser used for the subproblem (17b) of CSI feedback does not require SF2AD and AD2SF modules. Algorithm 4 describes the plug-and-play CSI feedback, i.e., PPPCF. Similarly, PPPCF can be used for any compression ratio since the denoiser is decoupled from the linear mapping that determines the compression ratio.

IV. EXPERIMENTEL RESULTS

This section evaluates the performance of the proposed method for the three tasks of channel estimation, antenna extrapolation, and CSI feedback.

A. Data Generation and Network Training

The dataset used in our experiments is generated by the DeepMIMO channel generation platform [36], which constructs MIMO channel data from accurate ray-tracing data obtained by the 3D ray-tracing software Remcom Wireless InSite¹ and different ray tracing scenarios and parameter sets can be used to achieve accurate definition and reproduction of the dataset. As shown in Fig. 3, the scene of this experimental data set is the outdoor scene "O1_28" with center frequency 28 GHz.

Referring to the setup in the literature [11], only BS3 is activated in this experiment, as shown in Fig. 3. The BS is equipped with a ULA² of 32 antennas and each UE has a single antenna. The system bandwidth is 200 MHz and the number of paths is 5. Users are placed in 3 uniform x-y grids, and this experiment activates the second user grid located in the south side of the street in Fig. 3, which contains 1101 rows, each row has 181 users. The interval between every two users is 20cm. 150,000 CSI samples were randomly selected as the dataset. The other parameters are shown in Table I.

The generated CSI samples are separated into the training dataset of 100,000 samples and validation dataset of 30,000 samples, which are used to train the denoising network, and the

TABLE I: DeepMIMO dataset simulation settings.

Parameters	Values
Scenarios	O1_28
Active BS	BS3
Active UEs	User Grid 2
Number of BS antennas	32
Number of UE antennas	1
UE sampling factor	0.8
Center frequency	28 GHz
Number of OFDMs	1024
OFDM sampling factor	1
OFDM limit	256
Number of paths	5

testing dataset of 20,000 samples, which is used to evaluate the proposed method. First, we normalize the power of the spatial-frequency domain CSI, and then add a random Gaussian noise uniformly generated in the range of $0 \sim 40$ dB, which produces the noisy spatial-frequency domain CSI. Next, the clean spatial-frequency domain CSI and the noisy spatial-frequency domain CSI are transformed to the angular-delay domain via DFT, and then truncated [14], [15], [17], [33], [37]–[39], i.e., only the first 32 rows of data are retained to obtain the final dataset. Each training sample contains the clean angular-delay domain CSI, the noisy CSI and the corresponding noise variance.

In the training phase, the batch size is set to 128 and the Adam optimizer is used. The denoising network is trained for a total of 200 epochs to converge, the learning rate is first set to 10^{-4} for initialization. When the loss is not reduced within 20 epochs, the learning rate will decrease by half, and the lower limit of the learning rate is set to 10^{-7} . In the evaluation phase, the remaining 20,000 samples are used to evaluate different performance of the proposed method and other comparison methods for different tasks. The proposed method is stopped after 10 iterations. Regularization parameter λ , penalty factor ρ , and scaling factor α can be fine-tuned and set to 0.5, 0.1, and 1.5, respectively.

¹<https://www.remcom.com/wireless-insite-em-propagation-software>

²The proposed method can also be applied to other types of antennas. Here we consider the ULA model for simplicity and fair comparison with other methods in literature.

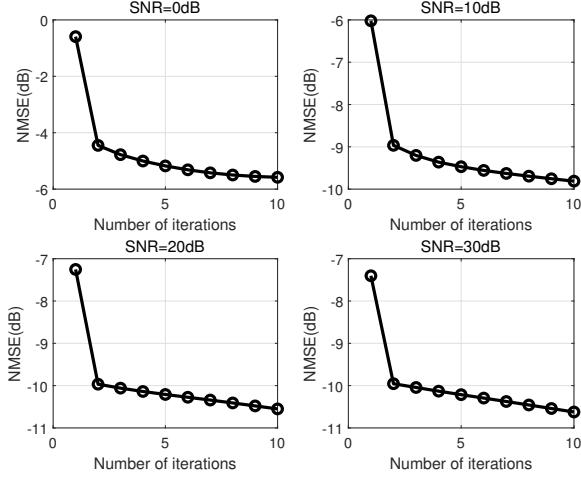


Fig. 4: The convergence of PPPCE with 128 pilots.

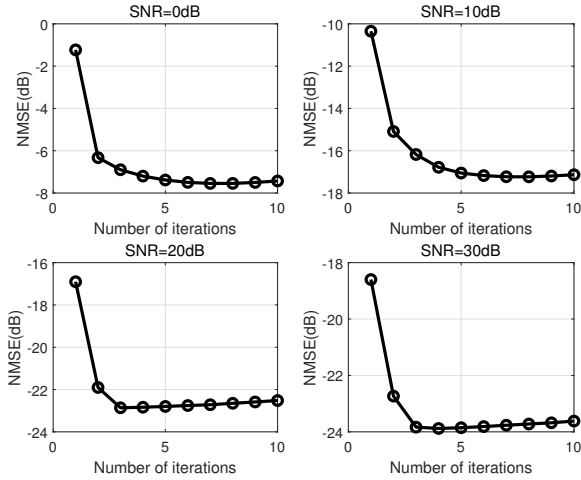


Fig. 5: The convergence of PPPCE with 256 pilots.

B. Performance of Channel Estimation

This subsection evaluates the PPPCE in terms of both convergence and channel estimation accuracy. The metric for assessing the channel estimation accuracy is the normalized mean-squared error (NMSE), which measures the difference between the recovered downlink frequency domain CSI, $\hat{\mathbf{H}}$, and the original downlink CSI, \mathbf{H} , and can be expressed as

$$\text{NMSE} = \mathbb{E} \left(\frac{\|\hat{\mathbf{H}} - \mathbf{H}\|_F^2}{\|\mathbf{H}\|_F^2} \right). \quad (30)$$

1) Convergence

The convergence of the current plug-and-play framework requires the denoiser to satisfy some mandatory properties that are usually not easy to DL-based denoisers, but extensive experiments have demonstrated that DL-based denoisers work well in the PPP framework [40]–[42]. This subsection shows the empirical convergence of PPPCE on the DeepMIMO dataset.

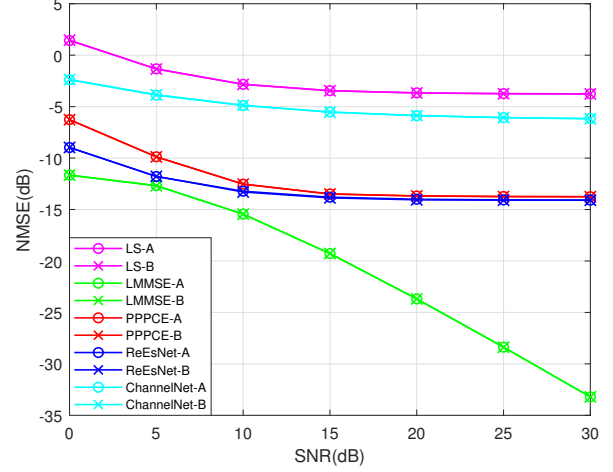


Fig. 6: Channel estimation accuracy of different methods with pilot number equal to 128.

The NMSE convergence curves of PPPCE on different samples with SNR of 0, 10, 20 and 30 dB are shown in Fig. 4 and Fig. 5 for pilot numbers of 128 and 256, respectively. It can be seen that the NMSE of PPPCE with different numbers of pilots all drops quickly in the first several iterations and then the decrease slows down in the subsequent iterations. Therefore, a few iterations would be sufficient to achieve good performance.

2) Channel Estimation Accuracy

Two classical channel estimation methods, i.e., LS and LMMSE [25], and two DL-based channel estimation methods, i.e., ChannelNet [10] and ReEsNet [25], are considered for comparison. It is worth noting that multiple models of ChannelNet and ReEsNet are trained for different pilot patterns. In contrast, the DL model of PPPCE is only for denoising, so a common DL model can be applied for all pilot patterns. In order to demonstrate that PPPCE is applicable to different pilot patterns, four pilot patterns A, B, C, and D are considered. 128 pilots with the pilot spacing 64 are considered for patterns A and B, and 256 pilots with the spacing 32 are considered for patterns C and D. Different patterns with the same spacing differ in the pilot positions. In addition, ChannelNet and ReEsNet use the dataset of hybrid SNRs, which is also used to train the denoiser of PPPCE.

Fig. 6 and Fig. 7 show the channel estimation accuracy for 128 and 256 pilots, respectively. From the figure, the LMMSE has the best accuracy because it uses the second-order channel statistics and noise variance as prior information, which is usually difficult to obtain in practice. Note that PPPCE requires only one DL model while ChannelNet and ReEsNet require four DL models, each of which is used for a specific pilot pattern. The performance of PPPCE is better than that of the ChannelNet and is very close to that of the ReEsNet.

C. Performance of Antenna Extrapolation

This subsection evaluates the performance of PPPAE.

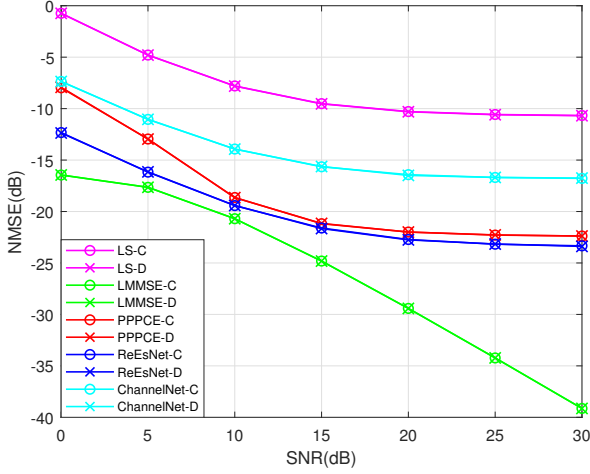


Fig. 7: Channel estimation accuracy of different methods with pilot number equal to 256.

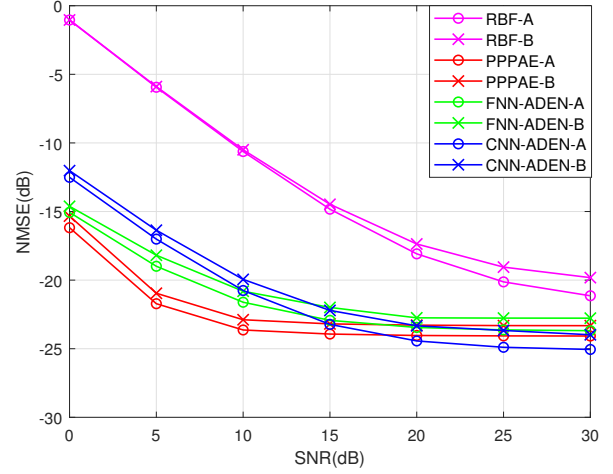


Fig. 9: Antenna extrapolation accuracy of different methods.

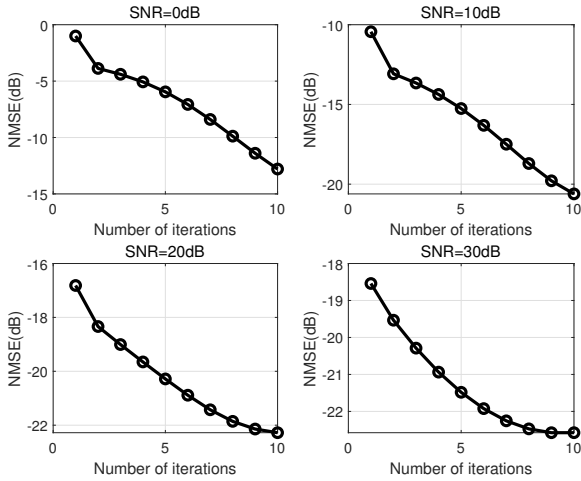


Fig. 8: The convergence of PPPAE.

1) Convergence

Fig. 8 shows the convergence curve of the NMSE of the PPPAE with 16 selected antennas and SNRs of 0, 10, 20 and 30 dB. From the figure, the NMSE decreases and converges at all the cases with different SNRs. Unlike PPPCE, the NMSE of PPPAE decreases slowly, and more iterations are required to achieve good performance in general.

2) Antenna Extrapolation Accuracy

In the antenna extrapolation task, the compared methods include spline interpolation, i.e., RBF, and DL-based ADEN [11] designed specifically for antenna extrapolation. Since ADEN consists of only fully connected layers with a large number of parameters, called FNN-ADEN in our paper, we further design a CNN-based network according to ADEN, namely CNN-ADEN. Note that FNN-ADEN and CNN-ADEN have fixed antenna selection patterns during training, so several DL models need to be trained for different antenna selection patterns. PPPAE is used for denoising, so it is not affected by the different antenna selection patterns.

Similar to the channel estimation task, two antenna selection

patterns with 16 antennas are designed, namely A and B, which indicates the selection of the odd-numbered antennas and even-numbered antennas. The antenna extrapolation accuracy of each method is shown in Fig. 9. The accuracy of the antenna extrapolation task differs with distinct antenna selection patterns. Furthermore, the accuracy of PPPAE is better than that of other methods at low SNRs. The DL model used in PPPAE and PPPCE is the same. The proposed approach enables the reuse of DL model for multi-tasks.

D. Performance of CSI Feedback

This subsection evaluates the performance of PPPC. In addition to the NMSE, another metric to evaluate the CSI feedback accuracy is the cosine similarity (CoS), which measures the quality of the beamforming vector, given as

$$\text{CoS} = \mathbb{E} \left(\frac{1}{N_s} \sum_{i=1}^{N_s} \frac{|\hat{\mathbf{h}}_i^H \mathbf{h}_i|}{\|\hat{\mathbf{h}}_i\|_2 \|\mathbf{h}_i\|_2} \right), \quad (31)$$

where $\hat{\mathbf{h}}_i$ and \mathbf{h}_i denote the recovered channel vector and the original channel vector of the i th subcarrier, respectively.

1) Convergence

According to (11), the compressed CSI, $\mathbf{A}\bar{\mathbf{h}}$, needs to be quantized for transmission. The quantization error is modeled as the noise term in (11). Fig. 10 shows the empirical convergence of the PPPCF with CR 1/8. There are five subplots, from left to right, representing different numbers of quantization bits. The results demonstrate the convergence of PPPCF in all cases.

2) CSI Feedback Accuracy

In the CSI feedback task, the proposed method is compared with the CS-based method, namely TVAL3 [43], and CsiNet+ [33], which is based on a two-sided CSI feedback framework that uses the DL model at both the UE side and the BS side.

Table II shows the CSI feedback accuracy of different methods under the DeepMIMO dataset. Five different CRs, i.e., 1/4, 1/8, 1/16, 1/32 and 1/64, are considered. "B" in Table II denotes the number of quantized bits. According to

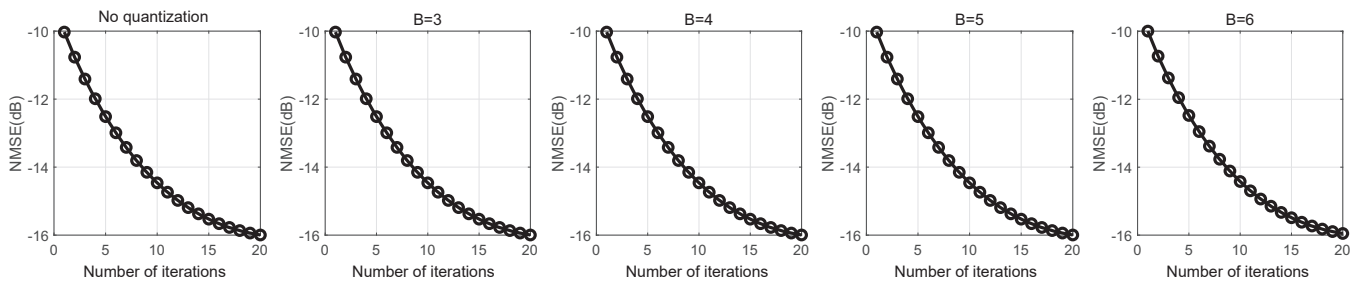


Fig. 10: The convergence of PPPCF.

the experimental results, the feedback accuracy of PPPCF is better than TVAL3 in all cases. When CR is 1/4, its feedback accuracy is close to CsiNet+ and even better under some quantized bits. In the remaining cases, the CsiNet+ achieves the best accuracy, which is understandable because the DL-based encoder at the UE side can extract more compact features than simple linear projections, especially when the CR is relatively low or the CSI structure is simpler. Moreover, the sensitivity of PPPCF to quantization bits is much lower than TVAL3 and CsiNet+. At CRs of 1/4, 1/8, and 1/16, the NMSEs increase by 1.44 dB, 1.84 dB, and 2.44 dB for CsiNet+, 4.48 dB, 1.49 dB, and 0.21 dB for TVAL3, and 0.07 dB, 0.24 dB, and 0.14 dB for PPPCF, respectively. This phenomenon is more significant at high CR, which indicates that PPPCF is more robust to the error caused by quantization.

E. Model Storage

This subsection discusses the model storage overhead of the other DL-based methods and the proposed method. Table III gives the number of model parameters required to implement each DL-based method for different communication tasks. It can be seen that the model storage overhead of the proposed method is much less than that of other DL-based methods. Specifically, for the channel estimation task with different pilot patterns, ChannelNet and ReEsNet have 1255.8K and 340.9K parameters, respectively. For the antenna extrapolation task with different antenna selection patterns, FNN-ADEN and CNN-ADEN have 27300.9K and 365.7K parameters, respectively. For the CSI feedback task with different CRs, CsiNet+ has 4095.4K parameters. In contrast, the DL model in the proposed method requires only 175.2K parameters, which is only 3.6% of model parameters in ReEsNet, CNN-ADEN and CsiNet+, to handle all the three tasks.

V. CONCLUSIONS

In this paper, we propose a novel multi-task method for massive MIMO systems, where a single DL model can be used for multiple communication tasks. Three downlink communication tasks are investigated, including channel estimation, antenna extrapolation, and CSI feedback. Using deep PPP, we developed PPPCE, PPPAE, and PPPCF for different tasks, which share a common DL model. The DL model does not require labeled dataset for different tasks, and the trained model can be reused in all tasks, which significantly reduces model training costs and model storage overhead. Extensive experiments show the advantages of the proposed method.

APPENDIX A

PROOF OF THE GLOBAL OPTIMAL SOLUTION OF (23)

(23) is an unconstrained optimization problem with the optimization terms $\|\mathbf{Y}_p - \mathcal{P}(\mathbf{H}) \circ \mathbf{X}_p\|_F^2$ and $\|\mathbf{Z}^t - \mathbf{H}\|_F^2$, which is a least squares optimization problem of the variable \mathbf{H} . There exists a global optimal solution and it makes (32) hold

$$\frac{\partial \left(\|\mathbf{Y}_p - \mathcal{P}(\mathbf{H}) \circ \mathbf{X}_p\|_F^2 + \rho \|\mathbf{Z}^t - \mathbf{H}\|_F^2 \right)}{\partial \mathbf{H}} = 0. \quad (32)$$

Since the transmitted signal at the non-pilot position is zero, the numerator on the left side of (32) can be divided into two sets \mathbb{P} and $\bar{\mathbb{P}}$ according to the pilot and non-pilot positions, which is shown as follows

$$\begin{aligned} & \frac{\partial \left(\|\mathbf{Y}_p - \mathcal{P}(\mathbf{H}) \circ \mathbf{X}_p\|_F^2 + \rho \|\mathbf{Z}^t - \mathbf{H}\|_F^2 \right)}{\partial \mathbf{H}} \\ &= \frac{\partial \left(\sum_{(i,j) \in \mathbb{P}} (y_{ij} - h_{ij} x_{ij})^2 + \rho \sum_{(i,j) \in \mathbb{P}} (h_{ij} - z_{ij}^t)^2 + \rho \sum_{(i,j) \in \bar{\mathbb{P}}} (h_{ij} - z_{ij}^t)^2 \right)}{\partial \mathbf{H}}, \end{aligned} \quad (33)$$

where h_{ij} , x_{ij} , y_{ij} , and z_{ij}^t denote the downlink spatial-frequency domain CSI, \mathbf{H} , the transmitted pilots \mathbf{X}_p , the received pilots \mathbf{Y}_p , and the result of the denoiser in the t th iteration \mathbf{Z}^t corresponds to the value of (i, j) position. If (33) is equal to zero, the closed-form solution of (23) is obtained by (34).

$$h_{ij}^{t+1} = \begin{cases} \frac{x_{ij} y_{ij} + \rho z_{ij}^t}{x_{ij}^2 + \rho}, & (i, j) \in \mathbb{P} \\ z_{ij}^t, & (i, j) \in \bar{\mathbb{P}}. \end{cases} \quad (34)$$

APPENDIX B

PROOF OF THE GLOBAL OPTIMAL SOLUTION OF (25)

(25) is also an unconstrained optimization problem and its global optimal solution makes (35) hold

$$\frac{\partial \left(\|\tilde{\mathbf{H}} - \mathcal{A}(\mathbf{H})\|_F^2 + \rho \|\mathbf{Z}^t - \mathbf{H}\|_F^2 \right)}{\partial \mathbf{H}} = 0. \quad (35)$$

Since only some of the antennas are selected, the numerator on the left side of (35) can be divided into two sets \mathbb{A} and $\bar{\mathbb{A}}$ by the set of selected antennas and the set of unselected antennas, which is shown as follows

$$\begin{aligned} & \frac{\partial \left(\|\tilde{\mathbf{H}} - \mathcal{A}(\mathbf{H})\|_F^2 + \rho \|\mathbf{Z}^t - \mathbf{H}\|_F^2 \right)}{\partial \mathbf{H}} \\ &= \frac{\partial \left(\sum_{(i,j) \in \mathbb{A}} (\tilde{h}_{ij} - h_{ij})^2 + \rho \sum_{(i,j) \in \mathbb{A}} (h_{ij} - z_{ij}^t)^2 + \rho \sum_{(i,j) \in \bar{\mathbb{A}}} (h_{ij} - z_{ij}^t)^2 \right)}{\partial \mathbf{H}}, \end{aligned} \quad (36)$$

TABLE II: Comparison of NMSE (dB) and GoS Performance in the DeepMIMO dataset

Method	CR		1/4	1/8	1/16	1/32	1/64
	B						
TVAL3	3		-8.86/0.84	-3.18/0.64	-1.20/0.49	-0.41/0.32	-0.12/0.21
	4		-11.35/0.91	-4.10/0.71	-1.37/0.54	-0.41/0.32	-0.12/0.21
	5		-12.76/0.94	-4.41/0.74	-1.40/0.55	-0.42/0.33	-0.12/0.21
	6		-13.34/0.96	-4.56/0.75	-1.41/0.56	-0.42/0.33	-0.12/0.21
	no quantization		-13.62/0.96	-4.67/0.75	-1.41/0.56	-0.42/0.33	-0.12/0.22
CsiNet+	3		-17.19/0.99	-16.25/0.99	-15.31/0.99	-14.01/0.98	-13.21/0.98
	4		-18.05/0.99	-17.39/0.99	-16.84/0.99	-16.11/0.99	-15.43/0.99
	5		-18.48/0.99	-17.87/0.99	-17.52/0.99	-17.13/0.99	-16.58/0.99
	6		-18.63/0.99	-18.09/0.99	-17.75/0.99	-17.54/0.99	-16.95/0.99
	no quantization		-18.72/0.99	-18.20/0.99	-18.07/0.99	-17.42/0.99	-17.18/0.99
PPPCF	3		-18.40/0.99	-13.44/0.98	-8.79/0.94	-4.29/0.82	-1.38/0.55
	4		-18.45/0.99	-13.59/0.98	-8.84/0.95	-4.57/0.84	-1.50/0.57
	5		-18.46/0.99	-13.65/0.98	-8.91/0.95	-4.70/0.84	-1.61/0.59
	6		-18.47/0.99	-13.67/0.98	-8.92/0.95	-4.73/0.84	-1.63/0.59
	no quantization		-18.47/0.99	-13.68/0.98	-8.93/0.95	-4.75/0.84	-1.64/0.59

TABLE III: Comparison of model storage overhead

Task	Method	Params
Channel Estimation	ChannelNet	1255.8K
	ReEsNet	340.9K
Antenna Extrapolation	FNN-ADEN	27300.9K
	CNN-ADEN	365.7K
CSI Feedback	CsiNet+	4095.4K
All The Three Tasks	PPPCE, PPPAE, PPPCF	175.2K

where h_{ij} , \tilde{h}_{ij} , and z_{ij}^t denote the downlink CSI, \mathbf{H} , the selected set of antennas corresponding to the downlink CSI, $\tilde{\mathbf{H}}$, and the result of the denoiser in the t th iteration \mathbf{Z}^t corresponding to the value of (i, j) position, respectively. If (36) is equal to zero, the closed-form solution of (25) is obtained by

$$h_{ij}^{t+1} = \begin{cases} \frac{\tilde{h}_{ij} + \rho z_{ij}^t}{1 + \rho}, & (i, j) \in \mathbb{A} \\ z_{ij}^t, & (i, j) \in \bar{\mathbb{A}}. \end{cases} \quad (37)$$

APPENDIX C PROOF OF (29)

First, we can perform SVD on the linear mapping matrix \mathbf{A} .

$$\mathbf{A} = \mathbf{U}\mathbf{\Sigma}\mathbf{V}^T \quad (38)$$

where $\mathbf{U} \in \mathbb{R}^{M \times M}$ and $\mathbf{V} \in \mathbb{R}^{N \times N}$ are unitary matrices. Note that it is explained in section II-C that the rows of \mathbf{A} are mutually orthogonal, so the first M columns of $\mathbf{\Sigma} \in \mathbb{R}^{M \times N}$ is a unit matrix and the rest of the columns are zeros. The partitioned matrix form of $\mathbf{\Sigma}$ is

$$\mathbf{\Sigma} = [\mathbf{I} \ \mathbf{0}], \quad (39)$$

where $\mathbf{I} \in \mathbb{R}^{M \times M}$ is a unit matrix and $\mathbf{0} \in \mathbb{R}^{M \times (N-M)}$ is an all-zero matrix. Combine (38) with (39), then $\mathbf{A}^T \mathbf{A}$ in (28) is expanded as

$$\mathbf{A}^T \mathbf{A} = \mathbf{V} \begin{bmatrix} \mathbf{I} & \mathbf{0} \\ \mathbf{0} & \mathbf{0} \end{bmatrix} \mathbf{V}^T. \quad (40)$$

Substitute (40) into (28) and (28) is further expanded as

$$\begin{aligned} \bar{\mathbf{h}}^{t+1} &= (\mathbf{A}^T \mathbf{A} + \rho \mathbf{I})^{-1} (\mathbf{A}^T \mathbf{y} + \rho \mathbf{z}^t) \\ &= \left(\mathbf{V} \begin{bmatrix} \mathbf{I} & \mathbf{0} \\ \mathbf{0} & \mathbf{0} \end{bmatrix} \mathbf{V}^T + \rho \mathbf{I} \right)^{-1} (\mathbf{A}^T \mathbf{y} + \rho \mathbf{z}^t) \\ &= \left(\mathbf{V} \left(\begin{bmatrix} \mathbf{I} & \mathbf{0} \\ \mathbf{0} & \mathbf{0} \end{bmatrix} + \rho \mathbf{I} \right) \mathbf{V}^T \right)^{-1} (\mathbf{A}^T \mathbf{y} + \rho \mathbf{z}^t) \\ &= \left(\mathbf{V} \begin{bmatrix} (1 + \rho) \mathbf{I} & \mathbf{0} \\ \mathbf{0} & \rho \mathbf{I} \end{bmatrix} \mathbf{V}^T \right)^{-1} (\mathbf{A}^T \mathbf{y} + \rho \mathbf{z}^t) \\ &= \left(\mathbf{V}^T \begin{bmatrix} \frac{1}{1 + \rho} \mathbf{I} & \mathbf{0} \\ \mathbf{0} & \frac{1}{\rho} \mathbf{I} \end{bmatrix} \mathbf{V} \right) (\mathbf{A}^T \mathbf{y} + \rho \mathbf{z}^t). \end{aligned} \quad (41)$$

REFERENCES

- [1] E. G. Larsson, O. Edfors, F. Tufvesson, and T. L. Marzetta, "Massive MIMO for next generation wireless systems," *IEEE Communications Magazine*, vol. 52, no. 2, pp. 186–195, 2014.

- [2] O. Elijah, C. Y. Leow, T. A. Rahman, S. Nunoo, and S. Z. Iliya, "A comprehensive survey of pilot contamination in massive MIMO-5G system," *IEEE Communications Surveys & Tutorials*, vol. 18, no. 2, pp. 905–923, 2016.
- [3] H. A. Ammar, R. Adve, S. Shahbazpanahi, G. Boudreau, and K. V. Srinivas, "User-Centric Cell-Free massive MIMO networks: A survey of opportunities, challenges and solutions," *IEEE Communications Surveys & Tutorials*, vol. 24, no. 1, pp. 611–652, 2022.
- [4] E. Onggosanusi, M. S. Rahman, L. Guo, Y. Kwak, H. Noh, Y. Kim, S. Faxer, M. Harrison, M. Frenne, S. Grant, R. Chen, R. Tamrakar, and Q. Gao, "Modular and high-resolution channel state information and beam management for 5G new radio," *IEEE Communications Magazine*, vol. 56, no. 3, pp. 48–55, 2018.
- [5] V. Ramireddy, M. Grossmann, M. Landmann, and G. D. Galdo, "Enhancements on Type-II 5G new radio codebooks for UE mobility scenarios," *IEEE Communications Standards Magazine*, vol. 6, no. 1, pp. 35–40, 2022.
- [6] V.-L. Nguyen, A.-C. Lin, B.-C. Cheng, R.-H. Hwang, and Y.-D. Lin, "Security and privacy for 6G: A survey on prospective technologies and challenges," *IEEE Communications Surveys & Tutorials*, vol. 23, no. 4, pp. 2384–2428, 2021.
- [7] B. Ozpoyraz, A. T. Dogukan, Y. Gevez, U. Altun, and E. Basar, "Deep learning-aided 6G wireless networks: A comprehensive survey of revolutionary PHY architectures," *IEEE Open Journal of the Communications Society*, vol. 3, pp. 1749–1809, 2022.
- [8] Moderator/Qualcomm, "New SI: Study on artificial intelligence(AI)/machine learning (ML) for NR air interface," Tech. Rep., 2022. [Online]. Available: http://3gpp.org/ftp/tsg_ran/TSG_RAN/TSGR_94e/Docs/RP-213599.zip
- [9] H. He, C.-K. Wen, S. Jin, and G. Y. Li, "Deep learning-based channel estimation for beamspace mmWave massive MIMO systems," *IEEE Wireless Communications Letters*, vol. 7, no. 5, pp. 852–855, 2018.
- [10] M. Soltani, V. Pourahmadi, A. Mirzaei, and H. Sheikhzadeh, "Deep learning-based channel estimation," *IEEE Communications Letters*, vol. 23, no. 4, pp. 652–655, 2019.
- [11] B. Lin, F. Gao, S. Zhang, T. Zhou, and A. Alkhateeb, "Deep learning-based antenna selection and CSI extrapolation in massive MIMO systems," *IEEE Transactions on Wireless Communications*, vol. 20, no. 11, pp. 7669–7681, 2021.
- [12] S. Zhang, S. Zhang, F. Gao, J. Ma, and O. A. Dobre, "Deep learning optimized sparse antenna activation for reconfigurable intelligent surface assisted communication," *IEEE Transactions on Communications*, vol. 69, no. 10, pp. 6691–6705, 2021.
- [13] M. Xu, S. Zhang, C. Zhong, J. Ma, and O. A. Dobre, "Ordinary differential equation-based CNN for channel extrapolation over RIS-assisted communication," *IEEE Communications Letters*, vol. 25, no. 6, pp. 1921–1925, 2021.
- [14] C.-K. Wen, W.-T. Shih, and S. Jin, "Deep learning for massive MIMO CSI feedback," *IEEE Wireless Communications Letters*, vol. 7, no. 5, pp. 748–751, 2018.
- [15] T. Wang, C.-K. Wen, S. Jin, and G. Y. Li, "Deep learning-based CSI feedback approach for time-varying massive MIMO channels," *IEEE Wireless Communications Letters*, vol. 8, no. 2, pp. 416–419, 2018.
- [16] J. Wang, G. Gui, T. Ohtsuki, B. Adebisi, H. Gacanin, and H. Sari, "Compressive sampled CSI feedback method based on deep learning for FDD massive MIMO systems," *IEEE Transactions on Communications*, vol. 69, no. 9, pp. 5873–5885, 2021.
- [17] Z. Hu, J. Guo, G. Liu, H. Zheng, and J. Xue, "MRFNet: A deep learning-based CSI feedback approach of massive MIMO systems," *IEEE Communications Letters*, vol. 25, no. 10, pp. 3310–3314, 2021.
- [18] Q. Cai, C. Dong, and K. Niu, "Attention model for massive MIMO CSI compression feedback and recovery," in *2019 IEEE Wireless Communications and Networking Conference (WCNC)*. IEEE, 2019, pp. 1–5.
- [19] Y. Wang, X. Chen, H. Yin, and W. Wang, "Learnable sparse transformation-based massive MIMO CSI recovery network," *IEEE Communications Letters*, vol. 24, no. 7, pp. 1468–1471, 2020.
- [20] Y. Jang, G. Kong, M. Jung, S. Choi, and I.-M. Kim, "Deep autoencoder based CSI feedback with feedback errors and feedback delay in FDD massive MIMO systems," *IEEE Wireless Communications Letters*, vol. 8, no. 3, pp. 833–836, 2019.
- [21] B. Zhang, H. Li, X. Liang, X. Gu, and L. Zhang, "Multi-Task training approach for CSI feedback in massive MIMO systems," *IEEE Communications Letters*, vol. 27, no. 1, pp. 200–204, 2023.
- [22] Z. Li, W. Gao, M. Zhang, and J. Xiong, "Multi-task deep learning based hybrid precoding for mmWave massive MIMO system," *China Communications*, vol. 18, no. 10, pp. 96–106, 2021.
- [23] Y. Han, T.-H. Hsu, C.-K. Wen, K.-K. Wong, and S. Jin, "Efficient downlink channel reconstruction for FDD multi-antenna systems," *IEEE Transactions on Wireless Communications*, vol. 18, no. 6, pp. 3161–3176, 2019.
- [24] X. Ru, L. Wei, and Y. Xu, "Model-driven channel estimation for OFDM systems based on image super-resolution network," in *2020 IEEE 5th International Conference on Signal and Image Processing (ICSIP)*. IEEE, 2020, pp. 804–808.
- [25] L. Li, H. Chen, H.-H. Chang, and L. Liu, "Deep residual learning meets OFDM channel estimation," *IEEE Wireless Communications Letters*, vol. 9, no. 5, pp. 615–618, 2019.
- [26] 38.211, "NR Physical channels and modulation (Release 17)," *3rd Generation Partnership Project (3GPP), Technical Specification*, 2022.
- [27] 38.212, "NR Multiplexing and channel coding (Release 17)," *3rd Generation Partnership Project (3GPP), Technical Specification*, 2022.
- [28] 38.213, "NR Physical layer procedures for control" (Release 17)," *3rd Generation Partnership Project (3GPP), Technical Specification*, 2022.
- [29] 38.214, "NR Physical layer procedures for data (Release 17)," *3rd Generation Partnership Project (3GPP), Technical Specification*, 2022.
- [30] S. Zhang, Y. Liu, F. Gao, C. Xing, J. An, and O. A. Dobre, "Deep learning based channel extrapolation for large-scale antenna systems: Opportunities, challenges and solutions," *IEEE Wireless Communications*, vol. 28, no. 6, pp. 160–167, 2021.
- [31] P. Dong, H. Zhang, and G. Y. Li, "Machine learning prediction based CSI acquisition for FDD massive MIMO downlink," in *2018 IEEE Global Communications Conference (GLOBECOM)*. IEEE, 2018, pp. 1–6.
- [32] L. Lu, G. Y. Li, A. L. Swindlehurst, A. Ashikhmin, and R. Zhang, "An overview of massive MIMO: Benefits and challenges," *IEEE Journal of Selected Topics in Signal Processing*, vol. 8, no. 5, pp. 742–758, 2014.
- [33] J. Guo, C.-K. Wen, S. Jin, and G. Y. Li, "Convolutional neural network-based multiple-rate compressive sensing for massive MIMO CSI feedback: Design, simulation, and analysis," *IEEE Transactions on Wireless Communications*, vol. 19, no. 4, pp. 2827–2840, 2020.
- [34] W. Chen, W. Wan, S. Wang, P. Sun, and B. Ai, "CSI-PPPNet: A one-sided deep learning framework for massive MIMO CSI feedback," *arXiv preprint arXiv:2211.15851*, 2022.
- [35] K. Zhang, W. Zuo, S. Gu, and L. Zhang, "Learning deep CNN denoiser prior for image restoration," in *Proceedings of the IEEE conference on computer vision and pattern recognition*, 2017, pp. 3929–3938.
- [36] A. Alkhateeb, "DeepMIMO: A generic deep learning dataset for millimeter wave and massive MIMO applications," *arXiv*, vol. 2019, no. 0, 2019. [Online]. Available: <http://dml.mathdoc.fr/item/1902.06435>
- [37] X. Li and H. Wu, "Spatio-temporal representation with deep neural recurrent network in MIMO CSI feedback," *IEEE Wireless Communications Letters*, vol. 9, no. 5, pp. 653–657, 2020.
- [38] X. Chen, C. Deng, B. Zhou, H. Zhang, G. Yang, and S. Ma, "High-accuracy CSI feedback with super-resolution network for massive MIMO systems," *IEEE Wireless Communications Letters*, vol. 11, no. 1, pp. 141–145, 2022.
- [39] Z. Lu, J. Wang, and J. Song, "Binary neural network aided CSI feedback in massive MIMO system," *IEEE Wireless Communications Letters*, vol. 10, no. 6, pp. 1305–1308, 2021.
- [40] K. Zhang, Y. Li, W. Zuo, L. Zhang, L. Van Gool, and R. Timofte, "Plug-and-play image restoration with deep denoiser prior," *IEEE Transactions on Pattern Analysis and Machine Intelligence*, vol. 44, no. 10, pp. 6360–6376, 2021.
- [41] M. Zhao, X. Wang, J. Chen, and W. Chen, "A plug-and-play priors framework for hyperspectral unmixing," *IEEE Transactions on Geoscience and Remote Sensing*, vol. 60, pp. 1–13, 2021.
- [42] E. Ryu, J. Liu, S. Wang, X. Chen, Z. Wang, and W. Yin, "Plug-and-play methods provably converge with properly trained denoisers," in *International Conference on Machine Learning*. PMLR, 2019, pp. 5546–5557.
- [43] C. Li, W. Yin, and Y. Zhang, "User's guide for TVAL3: TV minimization by augmented lagrangian and alternating direction algorithms," *CAAM report*, vol. 20, no. 46-47, p. 4, 2009.